



Research article

Coverage, repulsion, and reactivity of hydrogen on High-Entropy alloys

Frederik C. Østergaard^a, Frank Abild-Pedersen^b, Jan Rossmeisl^{a,*}^a Department of Chemistry, University of Copenhagen, DK-2100 Copenhagen, Denmark^b SUNCAT Center for Interface Science and Catalysis, SLAC National Accelerator Laboratory, Menlo Park, CA 94025, United States

ARTICLE INFO

Keywords:

Electrocatalysis
Density Functional Theory
Hydrogen Evolution Reaction
Simulation
Catalysis

ABSTRACT

Modeling hydrogen evolution reaction (HER) activity probability on IrPdPtRhRu(111) high-entropy alloys. Determining hydrogen coverages based on ligand effects and generalized hydrogen–hydrogen repulsion.

The rate of H₂ formation is highly impacted by the level of hydrogen coverage on the catalyst surface. In search of optimal catalytic properties high-entropy alloys (HEA) are promising candidates that utilize the compositional space of multiple elements. Based on simulations of HEA model (111) surfaces with a range of hydrogen coverages, distributions of binding energies are used to construct a framework that approximates the probability that adsorbed hydrogen may lead to the formation of H₂ as a function of applied potential. By optimizing the alloy compositions for the highest activity probability at given potentials the best and most efficient catalyst candidates for HER can be identified. Treating hydrogen–hydrogen repulsion effects and binding energy separately, we find that the repulsion is larger for HEAs than for pure metals. Differing isotherm slopes in the mean adsorption and desorption energies demonstrate a possible hysteresis for hydrogen adsorption on HEAs.

1. Introduction

More efficient and less expensive hydrogen evolution reaction (HER) catalysts are desirable to ensure feasible means for converting and storing intermittent renewable energy [1,2]. In recent years, multi-metallic catalysts known as high-entropy alloys (HEAs) have been the subject of an increasing number of studies (see Fig. SI-1), exhibiting promising properties for electrocatalysis [3–5]. The vast compositional space of multiple elements gives rise to numerous different surfaces that can be tuned for optimal catalytic activity or serve as a discovery platform [6]. However, as the combinatorics of multi-metallic compositions exceed practical scanning scales, particular search methods such as Bayesian optimization with Gaussian processes are often necessary [7].

Though HEA hydrides of early 3d transition metals have been studied for hydrogen storage, hydrogen coverage effects on HEAs in the scope of electrocatalysis have yet to be explored in-depth [8–11]. As adsorbate interactions on HEA surfaces is a continuously investigated field, it is relevant to study the effect of hydrogen coverage under operating conditions. It is tempting to assume that alloys of similar metals approach mean field properties according to the characteristics of the constituent metals. However, emergent properties and complex electronic

interactions may or may not be impacted by hydrogen coverage.

The level of hydrogen coverage on a pure metal catalyst surface is known to impact both the binding energy of adsorbates, adsorption configurations, and catalytic reaction mechanisms [12,13]. The effect on surface reactivity is proposedly not limited to hydrogen formation but also other chemical processes such as hydrogenation of organic molecules [14,15]. Changes in differential adsorption energies of hydrogen on Pt(111) of up to 0.2 eV have been demonstrated going from 1/9 ML to 1 ML hydrogen coverage [16]. For each of these degrees of coverage the most stable configuration is the one with the largest H–H distance, indicating repulsive adsorbate–adsorbate interactions which are not present in the less dense monolayers of (100) and (110) [17].

Whereas the general repulsion between surface hydrogen atoms is the obvious cause of changes to the adsorption energies on Pt(111), the heterogeneous nature of multi-metallic alloy surfaces suggests that local effects may play a significant role. When examining the local effects of hydrogen–hydrogen interactions on HEA surfaces one may consider the energies of adsorption of each hydrogen atom in a full monolayer, as illustrated by an example slab in Fig. SI-2a. In Fig. SI-2b the adsorption energies of the hydrogens on a probe IrPdPtRhRu (111) surface are shown to differ by up to 0.35 eV between the different sites (see Computational Details). Following BEP relationship between activation

* Corresponding author.

E-mail address: jan.rossmeisl@chem.ku.dk (J. Rossmeisl).<https://doi.org/10.1016/j.jcat.2024.115570>

Received 28 January 2024; Received in revised form 21 May 2024; Accepted 25 May 2024

Available online 27 May 2024

0021-9517/© 2024 The Author(s). Published by Elsevier Inc. This is an open access article under the CC BY license (<http://creativecommons.org/licenses/by/4.0/>).

energy and adsorption energy, only two sites (41 and 39) favor H adsorption to form a full monolayer, with the hydrogen at an IrRhRu site (46) being the least energetically favored for adsorption. Upon removing this hydrogen and calculating the changes in energy of adsorbing hydrogen to form an 11/12 monolayer, the majority still do not favor adsorption as most sites are almost unaffected by the change in coverage. Two adsorbed hydrogens are stabilized by the hydrogen desorption from the IrRhRu site (46), including the neighboring PtRuRu site (43). The nearest neighbor effect can be explained by decreased hydrogen–hydrogen repulsion.

The local effects on HEAs arise from the differences in the electronic environment surrounding the adsorption sites due to variations in atomic composition. As the model surfaces all have the same number of coordinating metals (both nearest and second-nearest neighbors), only the identity of each atom coordinating to the adsorption site plays a role [18,19]. The atoms coordinated directly to the adsorbate have the biggest influence on the binding energy [20]. For this reason, we focus entirely on the three metal atoms forming the hollow adsorption site, neglecting long-range and subsurface layer effects.

Whether the local interaction effects originate from the atomic identities or their coordination to the adsorption site, the formation of molecular H₂ relies on the prevalence of sites with weak adsorption energy. This is of high catalytic relevance as it helps drive the different steps of HER. Pt is known to be the superior catalyst for this reaction [21], however, due to its scarcity and price, HEAs may offer crucial understanding necessary to discover feasible alternatives [22]. Ideally, a good catalyst candidate would be composed of non-precious metals. However, to first gain a conceptual understanding of the effects of hydrogen coverage on HEAs, we choose a decently performing, yet precious HEA of IrPdPtRhRu as the model catalyst for this study.

1.1. Hydrogen evolution reaction

HER is a 2-electron process and one of the simplest electro-catalytic reactions. Its mechanism can be divided into two steps, the first being the Volmer step, the adsorption of protons onto the catalyst surface. Under alkaline conditions, where the proton concentration is low, the direct splitting of water is the source of protons, which is followed by adsorption of H⁺ through the Volmer step, adsorption of OH[−], or both.

Apart from interacting with each other, the hydrogen atoms on the catalyst surface may also affect the electrolyte as the interaction between the electrode and electrolyte is effectively screened by an increased hydrogen coverage. This may cause a greater distance between the protons in the electrolyte and the electrode surface, thus leading to higher energy barriers for adsorption. Recent studies on the coverage effect on Pt(1 1 1) in alkaline HER show substantial increases in electrode–water distances, and thereby alkaline hydrogen adsorption activation barriers, with increasing coverage of hydrogen [23]. AIMD simulations of this interface with Pt(1 1 1) and IrPdPtRhRu(1 1 1) HEA with 0 and 0.9 monolayer (ML) hydrogen coverage relative to the (1 1 1) surface show different water–electrode distances for the two electrodes. However, a similar difference is observed at increased coverage as the electrode composition is effectively screened when the hydrogen coverage approaches a full ML (see Fig. SI-3).

The second step of HER is H₂ formation either by the reaction of two adsorbed hydrogen atoms (Tafel step):



or by a proton from the electrolyte being reduced and reacting with an adsorbed hydrogen (Heyrovsky step):



In both mechanisms, adsorbed hydrogen is involved and hence the hydrogen–electrode interaction plays a crucial role in the HER kinetics. Depending on the catalyst composition and coverage, the free energy of

adsorption can be positive or negative when accounting for the difference in the entropic contribution and the zero-point energy between the adsorbed and the gas phase species (see Eq. (5)). When the free energy of adsorption is negative binding is said to be stronger making HER Heyrovsky or Tafel limited, whereas a weaker binding of hydrogen, i.e. positive adsorption, leads to HER being limited by the Volmer step and the activity of the catalyst then falls on the left or right leg of the Sabatier volcano, respectively [12,24,25]. The validity of this volcano-like hydrogen adsorption trend for HER has been questioned in recent studies, suggesting rather linear relationships [26]. In addition, dynamics of the electrified interface present activity criteria beyond the Sabatier principle [27]. Considering regressions of experimental HER overpotentials and simulated catalyst properties, the Sabatier volcano seems to be overlaid by a linear trend in work function [16]. However, as hydrogen adsorption energy remains the most important limitation to HER this study will focus mainly on the metals close to a ΔG of zero and on the “too strongly” binding side, for which the desorption step of H₂ formation is supposed rate-determining.

Assuming a BEP relationship between activation energy and adsorption energy for the Tafel step, the reaction rate is expected to increase with weaker adsorption energy [28,29]. While the proton concentration may impact the reaction rate in the regime of intermediate hydrogen adsorption energies, rendering water splitting important in alkaline conditions, on the left side of the Sabatier volcano the Heyrovsky step rate, too, relies on the prevalence of weaker hydrogen adsorption sites. Whether two hydrogens are adsorbed onto the surface, or a free proton reacts directly with an adsorbed hydrogen, the step requires an energetic net gain to form H₂.

In addition to the energetic requirement, for two adsorbed hydrogen atoms to react, they must also coordinate to each other within a reasonable distance. As strongly binding electrode surfaces tend to cover a layer of hollow site adsorbed hydrogen, the degree of hydrogen coverage may enter the equation as a measure of the probability of satisfactory coordination.

1.2. Computational details

DFT calculations were performed using the GPAW program package [30,31] with a setup of the RPBE exchange–correlation functional [32] and a plane wave (PW) basis set with a cutoff energy of 400 eV in the atomic simulation environment (ASE) [33]. The relaxations of the structures were carried out with convergence criteria of atomic forces: 0.05 eV Å^{−1}, total energy change: 0.0005 eV/electron, integral of absolute density change: 0.0001 electrons and integral of absolute eigenstate: 4 × 10^{−8} eV². Surfaces were modeled using the ASE package as 3 × 4 unit cells of three-layer slabs. For the initial relaxation of the slabs, the bottom layer was frozen at the DFT-calculated fcc lattice parameter. For hydrogen coverage, adsorption energy calculations, and water–electrode distance only metal atoms were fixated. Thus, all hydrogen atoms moved according to their forces. The *k*-point mesh used was 4 × 4 × 1 with Monkhorst-Pack mesh *k*-space sampling grids.

The hydrogen coverage calculations were carried out by sampling 100 (1 1 1) HEA compositions randomly generated from uniformly distributed probability ratios of each element. First adsorption energies were obtained from the 12 possible sites of the full hydrogen monolayer, while the following *n* adsorption energies of each descending hydrogen coverage were obtained from the 12-*n* possible sites in the conformation following the H removal from the highest energy site in the preceding coverage simulations.

The energies of adsorption were calculated using the equation:

$$\Delta E_{\text{H}^*} = E_{\text{H}^*} - E_{(n-1)\text{H}^*} - \frac{1}{2}E_{\text{H}_2} \quad (3)$$

where E_{H^*} is the energy of the slab with *n* adsorbed hydrogens, $E_{(n-1)\text{H}^*}$ is the energy of the slab with *n* − 1 adsorbed hydrogens, and E_{H_2} is the energy of molecular hydrogen in the gas phase.

Integral adsorption energies were calculated as:

$$E_{nH^+ \text{ int}} = E_{nH^+} - E^* - \frac{n}{2}E_{H_2} \quad (4)$$

where E^* is the energy of the pure slab. Differential adsorption energies, ΔE , were then obtained by finding the derivative with respect to n .

Free energies of adsorption, ΔG_{nH^+} were then calculated as:

$$\Delta G_{nH^+} = \Delta E_{nH^+} + \Delta E_{ZPE} - T\Delta S_H \quad (5)$$

where ΔE_{ZPE} is the difference in zero-point energy between the adsorbed and the gas phase and $T\Delta S_H$ is the entropic contribution. We use the gas

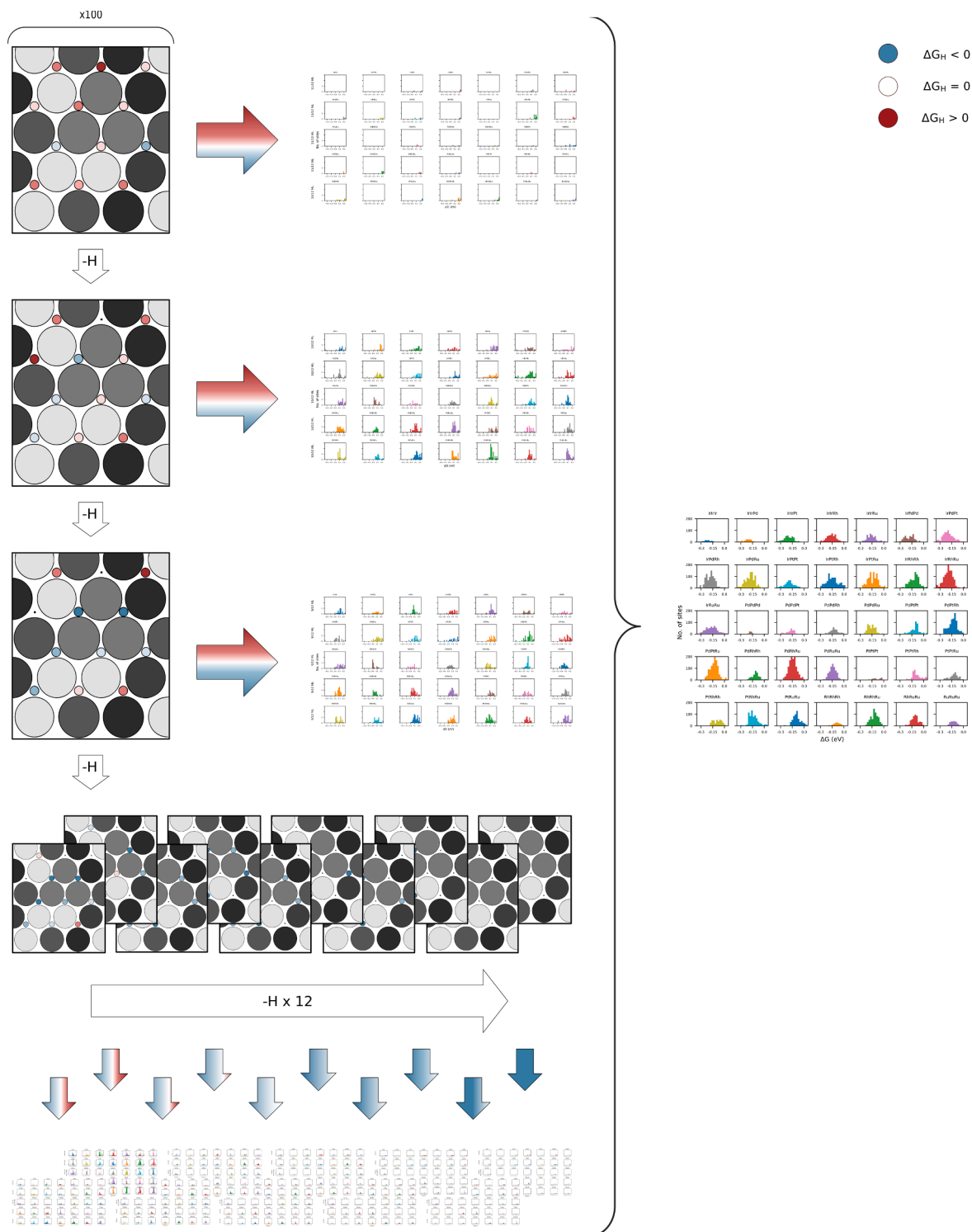


Fig. 1. Graphical representation of the adsorption energy sampling method employed in this study. Each surface frame represents the 100 randomly generated slabs at each degree of hydrogen coverage. The red and blue colors represent an adsorption energy colormap with weakest adsorption energy highlighted for each slab. Small inset histograms are distributions of hydrogen adsorption energies for each hollow site composition at each coverage and are given in larger scale in Fig. SI-9. The right histogram shows the collected, centered distribution and is given in larger scale in Fig. 5. (For interpretation of the references to color in this figure legend, the reader is referred to the web version of this article.)

phase values from Atkins [34] and adsorbed species values from Nørskov [25] yielding a free energy correction for H of 0.24 eV.

The Bayesian optimizations were carried out with squared-exponential kernel Gaussian process regressors with constant value and length scale hyperparameters of 0.05 and 0.5, respectively, as has previously shown suitable in a similar optimization study [7]. A standard choice of *expected improvement* as acquisition function was employed using an exploration–exploitation trade-off factor, x_i , of 4.0 for initially 10 random steps, then 150 optimization steps [35].

Data and scripts are available at https://chem.ku.dk/research_sections/nanochem/theoretical-electrocatalysis/.

1.3. Adsorption energy sampling

To study the probability of the Tafel step reaction, one must sample a range of adsorption energies from a sizable number of slabs. The sampling of hydrogen energies of adsorption was carried out by generating 100 different 3x4x3 (111) slabs of Ir, Pd, Pt, Rh, and Ru randomly drawn from a Dirichlet distribution with $\alpha = 1$ to ensure a uniform probability of sampling within the compositional space (See [Supporting Information](#) for extensive explanation) [36]. Reflecting the actual selection of adsorption and desorption sites when applying potential, the catalyst surface is expected to “fill up” from the most favorable adsorption sites first and likewise “empty” from the least favorable adsorption sites first. To obtain the adsorption energies at each degree of hydrogen coverage, firstly a full monolayer (ML) of 12 hydrogens was added to each slab, and the total energies were obtained by DFT calculations. Then 12 new calculations of each slab with 11/12 ML were performed by removing the H atom from each one of the 12 different available sites with adsorbed hydrogens. From the 11/12 ML structure with the lowest energy for each slab, 11 additional 10/12 ML calculations were run by removing one of the remaining 11 available hydrogens from the monolayer, respectively. Consistently selecting the lowest-energy structure with the given $n/12$ ML hydrogen coverage as the basis for the next $(n-1)/12$ ML calculations through to 0/12 ML, as visualized in [Fig. 1](#), yields data for determining the hydrogen adsorption energies for the 100 slabs (see Eqs. (3) and (5)). Similarly, calculations were carried out by consecutively adding hydrogens one at a time to the lowest-energy structure starting with the pure slab, yielding differential energies for adsorbing hydrogen ranging from coverages of 0/12 ML to 1 ML. This ensured that two times 100 times $\sum_{n=1}^{12} n$ (15,600 not considering duplicates) hydrogen coverage configurations were simulated, yet the full combinatorial multitude of configurations were not, as choosing the lowest-energy structure at each degree of coverage as the basis for the following structures excludes alternative combinations of sites.

For each of the 100 sample slabs and each degree of hydrogen coverage, the obtained energy change for adsorbing each specific H atom was then characterized by the three metal atoms constituting the hollow adsorption site. Three-fold combinations of five distinct elements give rise to 35 different sites, leading to 35 different distributions of adsorption energies for each hydrogen coverage. The sites consist of either three identical elements, two identical elements and a different third, or three different elements. These three cases have 1, 3, and 6 possible permutations, respectively, which is why the distributions should be weighted nominally by these factors.

1.4. Hydrogen adsorption isotherm

Plotting integral adsorption energies (see Eq. (4) with reference to the pure slab energies for each of the 35 unique adsorption sites as a function of the degree of hydrogen coverage demonstrates the free energy profiles of filling and emptying the HEA surface of hydrogen, as shown in [Fig. 2a](#). The values at each coverage are subjects to a biased selection when the adsorption energies are sampled for all possible sites before choosing the adsorption of the strongest binding H or the

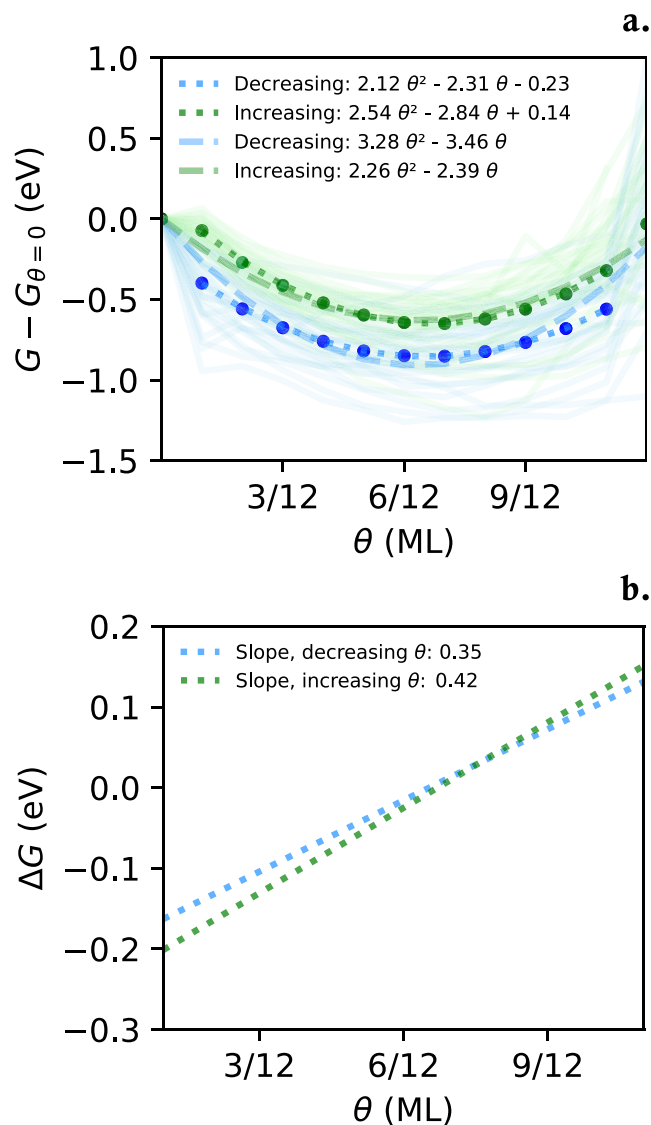


Fig. 2. Calculated average integral hydrogen adsorption energies with reference to the pure slab energies of each of the 35 different hollow-sites on IrPdPtRhRu HEA(111) as a function of hydrogen coverage. The opaque blue and green lines mark adsorption energies obtained by decreasing the coverage from a full monolayer and increasing the coverage from a clean surface, respectively. The dashed lines mark curve fits to weighted average values (darker colored dots) throughout the range of coverage, dotted lines mark the same omitting 0 ML and 1 ML. **b.** Frumkin isotherm of differential adsorption energies derived from the polynomial fits of (a) between 1/12 and 11/12 ML obtained by decreasing and increasing the hydrogen coverage. (For interpretation of the references to color in this figure legend, the reader is referred to the web version of this article.)

desorption of the weakest binding H as the next step for sampling. However, this selection is not applied to the pure slabs or the fully covered slabs. Naturally, there are no permutations to select at 0 ML and 1 ML coverage, as well as when adsorbing the last H at increasing coverage and when desorbing the last H at decreasing coverage. Considering the average values of all sites for each coverage, the first adsorption onto the pure slab as well as the first desorption from the fully covered slab represents no selection either. Therefore, curves are fitted to the average adsorption energies between 1/12 ML and 11/12 ML to model the integral adsorption energies as functions of coverage. The differences between the increasing and decreasing slopes seem larger at low coverages than at higher ones which is explained by the choice of reference at 0 ML coverage. Similar plots with references to

slabs at 1 and $\frac{1}{2}$ ML coverage are provided in Fig. SI-4. The derivatives of these functions with respect to coverage yield the differential adsorption energies as functions of coverage, what is known as a Frumkin isotherm. This isotherm highlights the impact adsorbate–adsorbate repulsion has on the adsorption energy, generally increasing the energetic cost of adsorption with increasing coverage, θ :

$$\Delta G = \alpha\theta + \beta \quad (6)$$

For pure metals the repulsion is in many cases approximated with the mean-field term only depending on overall coverage, as all sites on the surfaces are similar. This is not necessarily true for HEAs as the local electronic environment may differ depending on the adsorption site. Not all the sites display monotonously increasing average adsorption energies with increasing coverage. This is possibly due to configurational artifacts caused by the choice of unit cell such as hydrogen ring formation and hydrogen reconfiguring to on-top binding on Ir (see Fig. SI-5). Though hydrogen migration is neglected, histograms of hydrogen

distances from the initially optimized positions show some occurrence corresponding to on-top binding especially for Ir-abundant sites at low coverage in the decreasing-direction sampling (see Fig. SI-10). The on-top Ir binding energies are included in the Ir-abundant binding energy distributions. Subsurface atomic identities neglected in this study may also impact the adsorption energy distributions. Therefore, to find the repulsion effect, the adsorption energies for all possible sites must be averaged and weighted by their nominal occurrence to extract the repulsion effect, see Fig. 2b. Here, the nominally weighted average differential adsorption energies for each site on a 3x4 (111) surface of IrPdPtRhRu HEA are plotted for energies obtained by desorbing from a full monolayer going downwards in coverage as well as those obtained by adsorbing onto a clean surface going upwards in coverage. The difference in energy for these mean slopes arises from the sampling in which the choice of the next adsorption energy to calculate is determined by the previous choices dictated by the lowest-energy structure. Ultimately this purely thermodynamic treatment leads to discrepancy

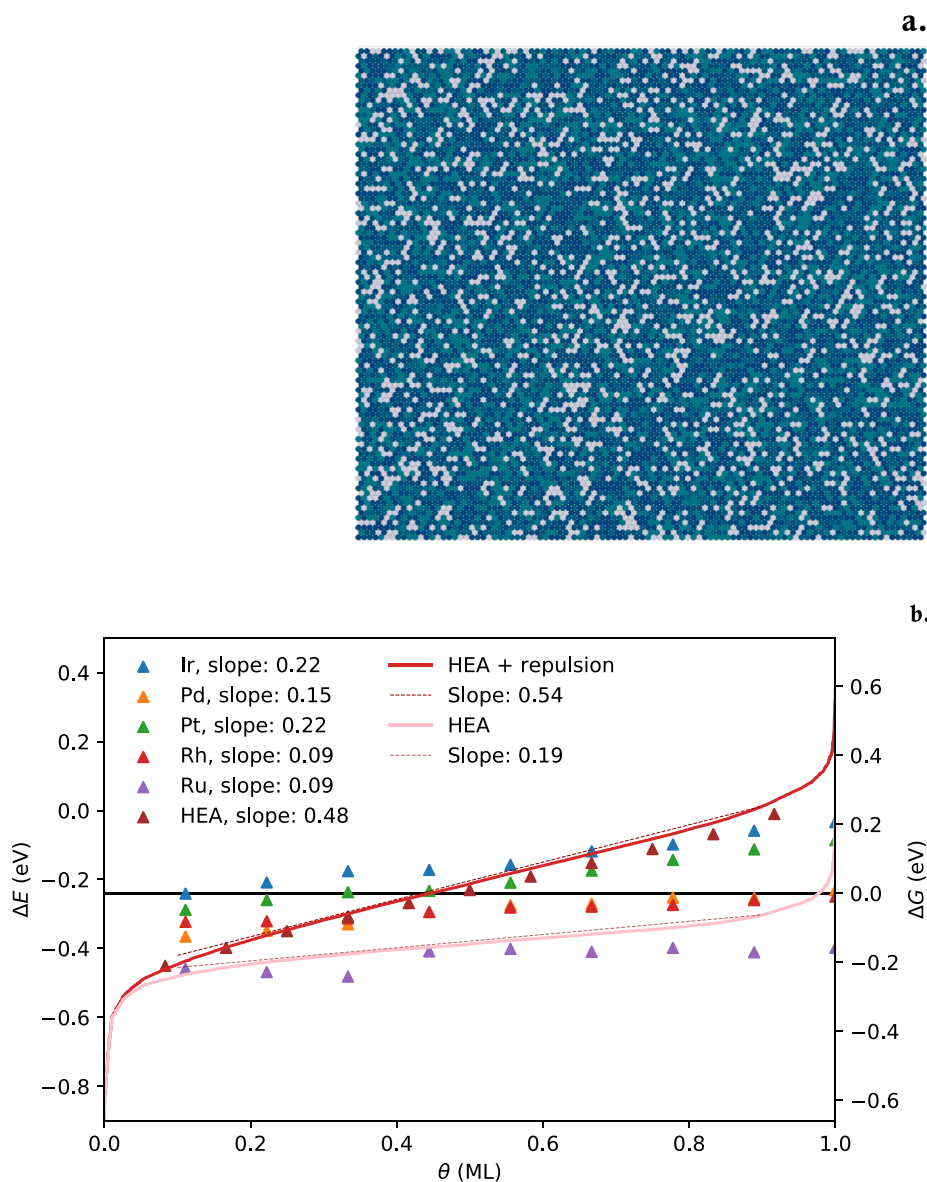


Fig. 3. Example of a 100x100 IrPdPtRhRu(111) HEA surface. **b.** Frumkin isotherms of the equimolar IrPdPtRhRu(111) HEA and (111) Ir, Pd, Pt, Rh, and Ru shown on ΔE and ΔG scales. Slopes are calculated as linear fits of the adsorption energies between 0.1 and 0.9 ML. Triangles mark single simulations. HEA single simulations are the corresponding adsorption energies sampled explicitly at $n/12$ ML coverage. Deviations from linear trends for the pure metals are due to configurational artifacts on the rather small-celled surfaces.

between which structures are evaluated when starting from high or low coverage. As an example, all of the 12 possible adsorption sites on the clean 3x4 surface available to reach 1/12 ML coverage are assessed when based on adsorption from zero ML coverage, whereas when studying the fully hydrogen-covered slab removing one hydrogen at a time, only one site remains to assess the adsorption energy at 1/12 ML coverage, and not necessarily the most energetically favorable one. We shall ignore the internal rearrangement of hydrogen on the surface and assume that this hysteresis mimics the experimental trends in HER electrocatalysis. In this study, the slope of change in adsorption energy by decreasing coverage is chosen as an expression for the repulsion effect, thus mimicking electrochemical experiments starting from strongly reducing potentials and scanning towards 0 V vs the standard hydrogen electrode (SHE).

Having obtained the mean repulsion effect for the equimolar IrPdPtRhRu(1 1 1) HEA as a function of hydrogen coverage, a complete Frumkin isotherm can be constructed using the sampled adsorption energies. As the adsorption energies are simulated at different coverages, they need to be normalized by centering them at 0 ML coverage. Treating the mean change in adsorption energy between each of the coverages examined in the sampling across all sites as a global “shift” in adsorption energy per 1/12 ML change in coverage, subtracting this shift times the number of hydrogens on the surface from the adsorption energies for each site at each sampled degree of coverage yields a pool of adsorption energies for each site centered at zero coverage. If an imaginary (1 1 1) layer of, e.g., 100x100 randomly selected atoms of Ir, Pd, Pt, Rh, and Ru (see Fig. 3a) were to be filled with a monolayer of hydrogen, each site can be assigned an adsorption energy drawn randomly from the pool corresponding to its atomic combination. Assuming the hydrogen will adsorb onto the sites in ascending order of adsorption energy, the index of each of the 10,000 adsorption energies sorted from low to high corresponds to the hydrogen coverage in terms of 10,000th fractions. When the adsorption energies are then plotted as a function of hydrogen coverage, a Frumkin isotherm emerges, as seen as the pink line in Fig. 3b. This inverse cumulative distribution function reflects the Gaussian-like distribution of adsorption energies as the extrema diverge symmetrically towards the few outliers. In contrast, most of the values are drawn from the denser middle section of the distribution, causing the isotherm to appear linear except for the edges.

To account for the hydrogen–hydrogen repulsion experienced with increasing coverage, the slope of mean change in adsorption energies times the degree of coverage is added as a repulsion function, as shown by the red line in Fig. 3b. The chemical potential for the Volmer step is given by $\Delta G_H = -eU$, and since one electron is transferred the free energy of adsorption is proportional to the negative applied potential [28,37]. This isotherm can be interpreted as the actual Frumkin isotherm describing the observed hydrogen coverage at a given applied potential corresponding to an adsorption energy on the free energy scale (see Eq. (5) [38]). The repulsion-corrected isotherm shows hydrogen underpotential deposition (HUPD) as expected. The hydrogen adsorption energies of the pure metal (1 1 1) constituents of the HEA are also plotted at coverages 1/9 through 1 ML obtained from simulations of 3x3 slabs. The slopes vary from 0.09 to 0.22 exhibiting low repulsion compared to the 0.35 slope of the HEA repulsion function. One explanation for the inherently stronger repulsion effect on the HEA in this simulation is that the hydrogens fill up the surface depending only on the adsorption energy, not on minimizing the hydrogen repulsion. On pure metal surfaces, the lowest energy configuration will always be the one with the least amount of repulsion. Still, for HEAs, the lowest energy may be found by adsorbing a hydrogen in an electronically favorable site, though not necessarily the site with the maximal hydrogen–hydrogen distance minimizing repulsion.

In Fig. 3b points are also plotted showing the individual simulations of IrPdPtRhRu HEA adsorption energies corresponding to the adsorption occurring at 1/12 through 11/12 ML coverage simulated with explicit coverage. These points reflect the isotherm obtained by calculating the

different coverages independently thus not applying a general repulsion effect. Therefore, these simulations include both the ensemble and ligand effects undistinguishably, unlike the zero-coverage centered isotherm with separate general repulsion. As this difference does not seem to give rise to any substantial change in the isotherm the separation of effects is validated.

1.5. Model design

After obtaining a large number of hydrogen adsorption energies and determining a coverage function from sampling HEAs, a reaction probability model can be constructed. In brief, the model in this study is based on estimating the probability of two hydrogens adsorbed on a given HEA surface to react and form H_2 , assuming no energy barrier. I.e., the model provides a measure for a site on a given HEA surface to be active at a given potential. This is done by first collecting the adsorption energies into a distribution that is weighted according to molar fractions and the nominal occurrence of each hydrogen site. From this distribution, the probability of drawing two hydrogens with a positive net sum free energy can then be approximated iteratively and the probability of forming H_2 determined.

With the adsorption energy distributions prepared, they must be centered at zero coverage by subtracting the mean change in adsorption energy between each of the coverages sampled for each site. The centered distributions can then be shifted towards a given coverage by adding increments of the mean adsorption energy shift. Having expressed a Frumkin isotherm with a generalized repulsion effect for the structure, the coverage at a given potential is simply obtained as the function value of the inverse isotherm.

Now, the data set is ready for determining the probability of H_2 formation at a given potential. The potential, U_0 , sets the upper boundary for what adsorption energies in the data set are available, as the hydrogens corresponding to adsorption energies higher than the applied potential are not adsorbed.

From the remainder of the distribution, two values are drawn and summed to determine the nature of the outcome: a positive sum corresponds to the energetic possibility of H_2 formation whereas a negative sum corresponds to retained adsorption of the hydrogens. The probability of H_2 formation can now be evaluated from the energies using a Monte Carlo method, continuously drawing random values, and determining the rate of a positive outcome, r_p , until a certain level of convergence has been reached:

$$r_p = \frac{N_{\sum(\Delta G) > 0; \Delta G < U_0}}{N_{\Delta G < U_0}} \quad (7)$$

where $N_{\sum(\Delta G) > 0; \Delta G < U_0}$ is the number of draws from energies, ΔG , larger than the applied potential yielding a positive energy sum, $\sum(\Delta G)$, and $N_{\Delta G < U_0}$ is the total number of draws from energies below the applied potential, see Fig. 4. This rate accounts for the energetic feasibility of the reaction.

However, to estimate the probability of reaction one must also consider the coordination of the participating hydrogen atoms. Therefore, the chance of the two drawn hydrogen atoms being next to each other must be included in the equation. This is ensured by scaling with a factor of the squared hydrogen coverage, θ^2 , obtained from the isotherm at each given potential.

The total probability as a function of applied potential is then given by:

$$p(U) = \theta(U)^2 \cdot r_p \quad (8)$$

For the Monte Carlo evaluation of this model, iterations of random samples of two available adsorption energies are continuously drawn and assessed, leading to new probabilities. The iterations are done when the numerical difference between a new probability and the previous is below the convergence threshold which was 10^{-5} . See Fig. SI-6 for

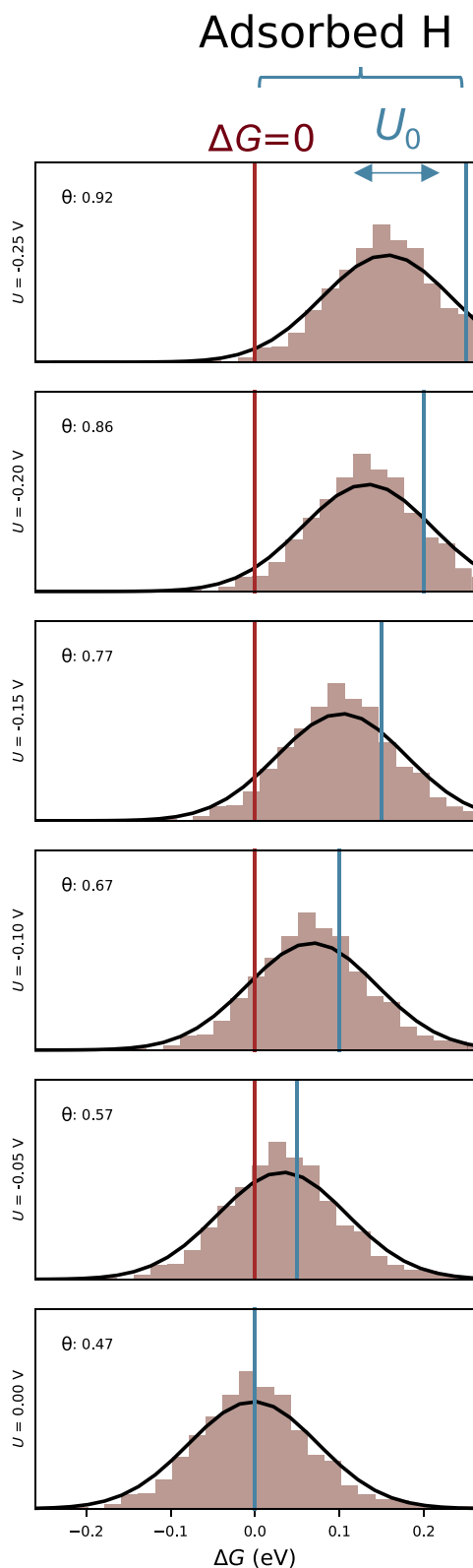


Fig. 4. Distributions of hydrogen adsorption energies for each hollow site on 100 samples of IrPdPtRhRu(111) surfaces divided into histograms for each degree of hydrogen coverage corresponding to a given applied potential. ΔG refers to the differential adsorption energy. Red line marks a free energy of 0, which the sum of two hydrogen adsorption energies needs to be above for H_2 formation to be energetically possible. Blue line marks the negative applied potential, to the left of which adsorption energies are available for random draws. (For interpretation of the references to color in this figure legend, the reader is referred to the web version of this article.)

convergence graphs. Given a range of applied potentials, a graph can be drawn expressing the probability of the Tafel reaction as a function of potential for a given HEA composition. This composition can be tuned for optimal probability at a particular potential using Bayesian optimization with Gaussian processes as described in the computational details [7].

2. Results and discussion

Upon sampling the hydrogen binding energies at different coverages, the increments of change in differential adsorption energy suggest an approximate linear increase in adsorption energy with increasing coverage with a few exceptions (see Fig. SI-5a). When inspecting the individual sites, the isotherm graphs reveal almost complete monotonous increases, justifying the assumption of a general repulsion effect. For the reaction probability model, the adsorption energy distributions are therefore centered at zero hydrogen coverage and the repulsion enters the model as a general linear function. The obtained centered distributions of adsorption energies divided into the 35 different site identities are shown in Fig. 5. However, there is a difference between simply averaging the distributions to a mean-field and considering repulsion and ligand effects separately. In this study, repulsion is described as a general effect obtained from a linear regression of mean adsorption energies at specific coverages, while the ligand effect, or local electronic environment, is treated individually by site, but averaged with respect to coverage and centered at 0 ML. This way the coverage at a given potential can be found using both binding energies dependent on atomic composition, regardless of repulsion, and the generalized repulsion effect, which can also be tuned according to the molar fractions of the composite metals.

In addition to being dependent on catalyst composition, the generalized repulsion function observed in Fig. 2 is also affected by the direction of the applied catalytic potential – whether the hydrogens are removed from the full monolayer or adsorbed one by one onto the clean surface. In each case, some configurations are left out as the lowest energy site of each previous step is chosen as the basis for the next step. Viewing the path from either end of the coverage scale to the other in terms of a potential energy surface, this methodology ensures the steepest descent from each configuration to the next, but not necessarily the lowest energy destination. Though being an artifact of our proposed scheme and not purposely describing an observed trend, this effect could explain if hysteresis was observed in a hydrogen evolution experiment on HEAs. It showcases a consequence of the ligand effect in HEAs that is not present in pure metal surfaces. Furthermore, it highlights the interplay between ligand and repulsion effects which lead to an inherent increased repulsion for highly heterogeneous surfaces as local electronic environments favor different adsorption sites rather than the ones required for the maximal hydrogen–hydrogen distance.

The constructed reaction probability model was initially run on the equimolar HEA at potentials ranging from -0.25 V to 0 V vs SHE with 0.01 V intervals. This composition yielded an expected decreasing reaction probability pattern as the potentials approach zero, following a slightly concave graph as seen in Fig. 6a. Along with equimolar HEA reaction probability the pure metals Ir, Pd, and Pt are plotted described solely by their squared values of hydrogen coverages as functions of potential, thereby assuming a 100 % rate of energetic feasibility, r_p . This stems from the assumption that the hydrogen binding energy on pure metals solely depends on the degree of hydrogen coverage and thereby does not adhere to any local effects. This leads to an absence of binding energy distributions as each potential and coverage therefrom derived gives rise to one discrete binding energy. While this value is negative, the rate of energetic feasibility will be 1, and the probability of reaction thus be given by the squared coverage. The discrete binding energies of pure metals also suggest no cut-off from the pool of adsorption energies when drawing randomly, as opposed to the adsorption energy distributions of HEAs which can extend beyond the given potential and

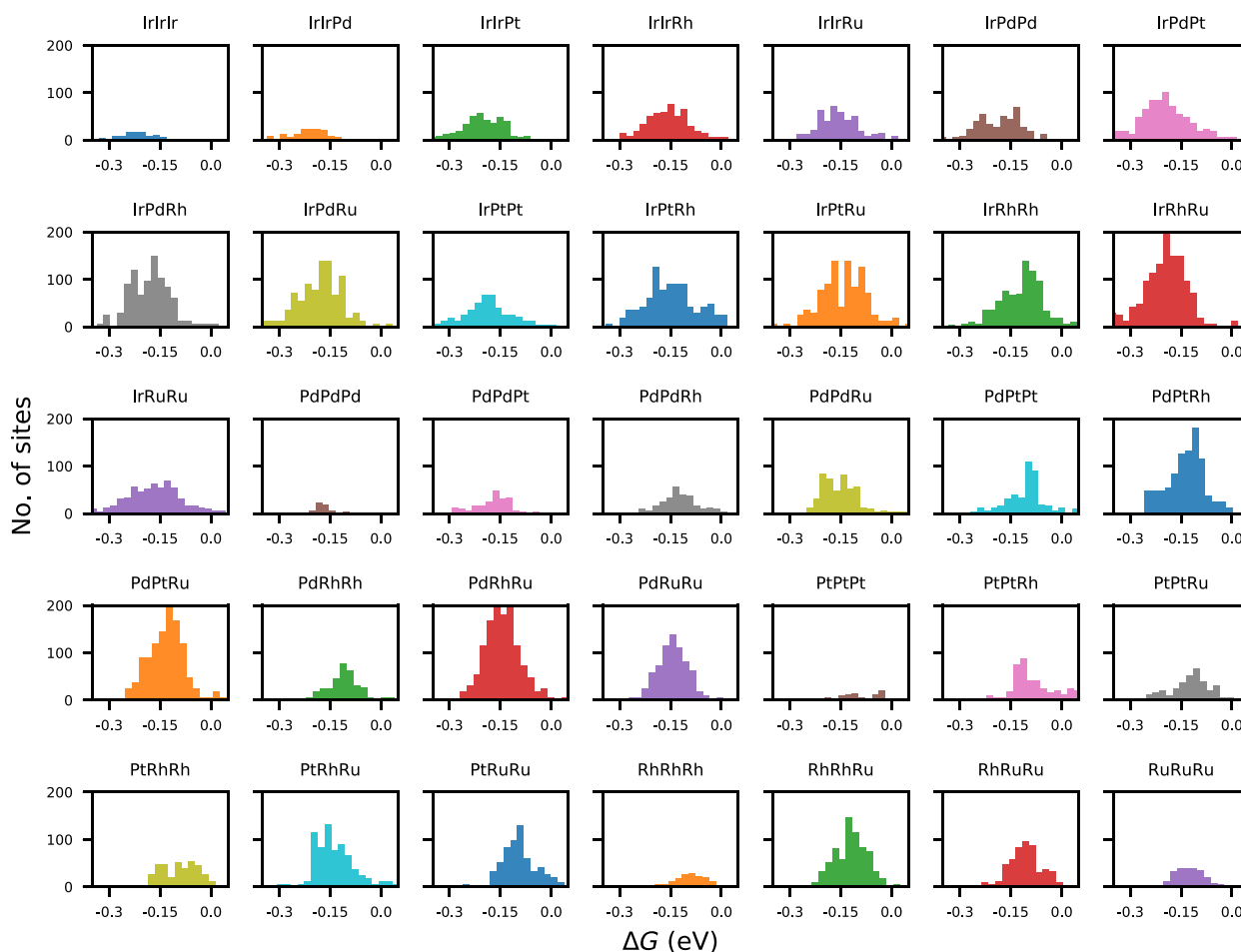


Fig. 5. Distributions of hydrogen adsorption energies for each site on the 100 samples of IrPdPtRhRu(111) surfaces divided into histograms for each hollow site composition. The histograms are weighted by number of possible permutations. Upon subtraction of the average shift in adsorption energy between each degree of coverage, the distributions of adsorption energies are centered at 0 ML. From here, the general repulsion effect can be added to reflect the coverage according to a given applied potential.

therefore be inaccessible. As the pure Ir, Pd, and Pt reach a full monolayer of hydrogen coverage at relatively low negative potentials, the model soon predicts their reaction probability to be 1. The abrupt switch from zero to 100 % rate of energetic reaction feasibility is an artifact in this framework due to the discrete adsorption energies of pure metals. As only hydrogen coverage impacts the adsorption energies, Pd has a high reaction probability at a very high coverage. But when the reaction occurs and H_2 is formed, the coverage falls, adsorption energies decrease, and the reaction probability drops to zero. That is until a new proton adsorbs and the reaction is feasible again. Therefore, due to the discrete nature of the model and its handling of HUPD, theoretically only one site in the unit cell can be active. Previous experimental studies find Pt more HER active than Pd [24,39,40]. In this light, the site activity probability does not directly translate into HER reactivity as a reasonable share of sites being active may sufficiently facilitate high exchange current.

Isolating active sites in alloy surfaces has, though, been shown to improve catalytic activity for other electrochemical reactions more dependent on selectivity than HER [41,42].

In the cases of Rh and Ru, even at zero potential, the hydrogen coverage has already reached a full monolayer and the adsorption energies are all negative. While approximating the reaction probability of pure metals directly from their hydrogen coverage squared identifies known well-performing catalysts, it may not be the most appropriate model for HER on pure metals, keep in mind the model only accounts for the Tafel step of the reaction and does not handle degrees of coverage

above 1 ML.

However, the model proves beneficial for screening potential new catalysts by exploring the compositional space of HEAs. By effectively predicting reaction probabilities at given applied potentials for any molar fractions within the constructed IrPdPtRhRu framework, the model is suitable for parameter optimization to search for high reaction probability. This was done by performing Bayesian optimization with squared-exponential kernel Gaussian process regressors at various potentials: 0.20 V, 0.15 V, 0.10 V, and 0.05 V. Following an algorithm choosing 10 initial random compositions to map out reaction probability space, the optimization continuously chose regions with the least exploration and regions with the highest performance expectations to assess until a maximum of 150 runs were completed. To focus the search on the edges and interior of the compositional space, molar fractions for each metal were restricted to below 0.80. The optimal composition for the given applied potential was then selected and modeled at potentials ranging from -0.25 V to 0 V vs SHE with 0.01 V intervals. It is worth noting that some of the optimized compositions are optimal in only a narrow potential window (see Fig. SI-8).

As shown in Fig. 6b the optimized catalysts tend to be of binary or ternary compositions yielding significantly higher reaction probabilities than the quinary equimolar composition. Unsurprisingly, well-known HER catalyzing metals Pd and Pt dominate the low-potential realm in terms of optimal compositions, which though not a novel finding supports the credibility of the model. However, one should be wary when considering alloys at the edges and corners of the compositional space as

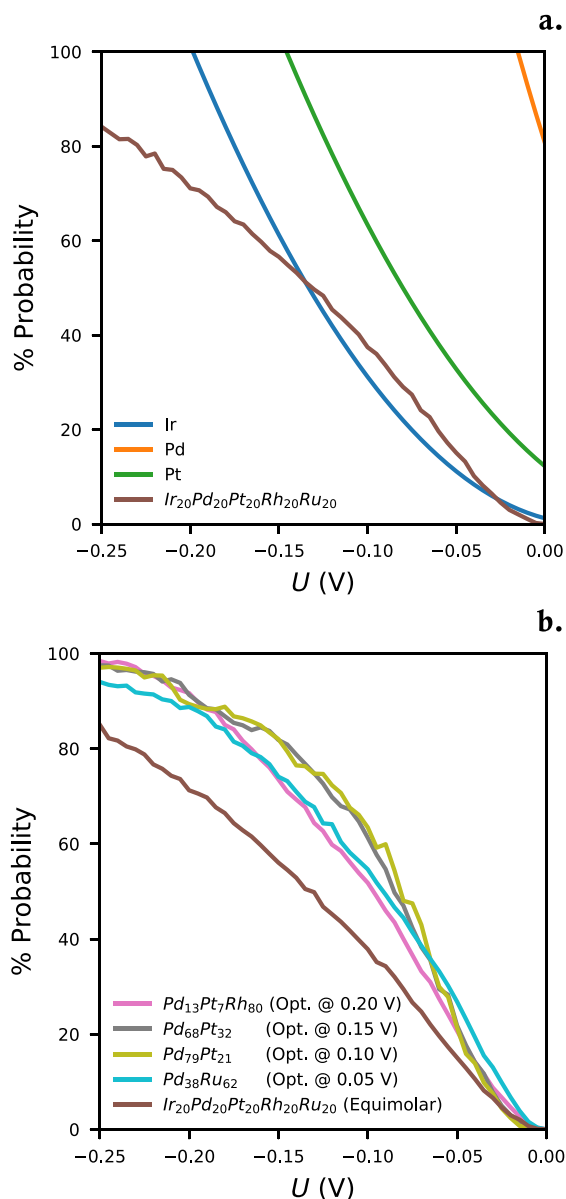


Fig. 6. Probability model results of applied potentials between -0.25 V and 0 V on the equimolar IrPdPtRhRu HEA as well as the pure metals Ir, Pd, and Pt. Note that the rate of energetic feasibility is 1 for pure metals when the adsorption energies are positive, as they are discrete values equal for all sites rather than distributions. As coverage determines the adsorption energies for pure metals, reaction at very high coverage and slightly positive adsorption energies is limited to few active sites as the adsorption energies drop upon reaction. **b.** Probability model results of applied potentials between -0.25 V and 0 V on compositions optimized for -0.20 V ($\text{Pd}_{13}\text{Pt}_7\text{Rh}_{80}$), -0.15 V ($\text{Pd}_{68}\text{Pt}_{32}$), -0.10 V ($\text{Pd}_{79}\text{Pt}_{21}$), and -0.05 V ($\text{Pd}_{38}\text{Ru}_{62}$).

bulk effects otherwise not present in the sampled HEAs may be overlooked. This might be relevant in the case of alloys with high molar fractions of Pd, as pure Pd is known to form hydrides [43]. Pt hydrides have also been shown to form, but at high pressure [44,45]. This hydride formation is not directly accounted for in our model. The sampling did, however, include Pd-abundant adsorption sites simulated at high hydrogen coverage, which to some extent incorporates surface hydrides. As higher hydrogen coverage was shown to increase adsorption energy, this at least matches the direction of the impact of hydride formation on the adsorption energy. For alloys with lower Pd content such as the activity optimum at 0.20 V, $\text{Pd}_{13}\text{Pt}_7\text{Rh}_{80}$, and Pd-Pt alloys containing more than 20% Pt hydride formation is negligible [46].

One would expect some Ir presence among the high-performance binaries and ternaries as well. Though well suited for HER due to its intermediate hydrogen binding energy, the absence of Ir in the optimal compositions is explained by its relatively low degree of hydrogen coverage at operational potentials. In Fig. 3b, pure Ir shows around $\frac{1}{4}$ ML coverage at 0.05 – 0.10 V potentials, which would probably also push an Ir-abundant HEA towards lower coverage, thus negatively impacting the reaction potential. This is also evident in Fig. 6a, where the low hydrogen coverage of pure Ir causes the reaction probability to drop below the equimolar HEA for potentials between -0.13 V and -0.03 V.

At very low potentials, Ru suddenly emerges as the main component of the optimal composition. This may seem improbable at first as pure Ru does not have any positive adsorption energies within the first full monolayer of coverage. However, considering the 35 different hollow sites constituting the binding energy distributions, the inclusion of one or two Ru atoms in a site may not be enough to deactivate the hydrogen desorption effectively. Namely in the case of $\text{Pd}_{38}\text{Ru}_{62}$ most accessible sites include Pd, too, balancing the binding energy distribution, while benefitting from the high hydrogen coverage of Ru even at low potentials. Though a fair amount of the sites present in $\text{Pd}_{38}\text{Ru}_{62}$ surfaces may be purely constituted by Ru, the binding energies sampled for RuRuRu sites in this study include the likely heterogeneous subsurface nature of HEAs, as opposed to the pure Ru simulations. Furthermore, it is worth recalling that the model only considers active sites for the Tafel step, and as such cannot directly mirror our expectations for HER activity for all catalysts. Considering uniform surfaces, the hydrogen–hydrogen distances between neighboring hollow-sites are unrealistic for reaction. However, the heterogeneity of the HEA surface causes some sites to bind hydrogens considerably weaker than others which facilitates increased mobility of the weakly bound hydrogen. Though Ru is more oxophilic, our model does not consider OH adsorption, which may play a role in alkaline HER [47]. This has recently been observed on bimetallic single-atom catalysts [48] and on steps and edges of slab surfaces while H adsorption dominates the (111) terraces [16]. However, OH adsorption energy simulations were carried out for a slab of the 0.05 V-optimal $\text{Pd}_{38}\text{Ru}_{62}$ composition ($\text{Pd}_{14}\text{Ru}_{22}$) with $11/12$ ML H coverage as well as for a single slab of random equimolar probability composition ($\text{Ir}_5\text{Pd}_6\text{Pt}_9\text{Rh}_7\text{Ru}_9$) both showing free energies of OH adsorption above 0.5 eV thus not adsorbing at operating conditions (see Fig. SI-7).

A grid search of all compositions with molar fraction steps of 0.05 was also completed for the applied potentials 0.10 V, 0.07 V, and 0.05 V to trawl for any possible overlooked probability peaks and gain a deeper understanding of the shift towards Ru abundant catalysts when approaching 0 V. The results of the searches are plotted as pseudo-ternary heatmaps in Fig. 7, in which Ir, Rh, and Ru have been combined for visual clarity. The search found no probability peaks different from the Bayesian optimization, however, the heatmaps do highlight the importance of stronger-binding metals to ensure higher hydrogen coverage at low potentials for optimal Tafel reaction probability. It is also worth noting that at 0.10 V, though a high concentration of Pt is predicted to lead to minimal reaction probability, a molar fraction of 0.15 – 0.20 Pt in a binary alloy with Pd yields the highest model score. In general, the trend in the results of this probability model suggests that optimal performance is achieved by tuning known good pure metal catalysts like Pd by alloying it with additional metals to yield a higher degree of coverage and a denser distribution of hydrogen adsorption energies between the applied negative potential and 0 V – effectively rendering the apex of the hydrogen adsorption volcano slightly on the weakly binding side as proposed by a recent study [49]. A finding regarding tuning towards the peak of the Sabatier volcano has been published by Batchelor et al. [6].

Having designed and proven the model methodology concept, less expensive and scarce metals like the 3d transition metals may lead to more economically feasible alternatives to precious metal catalysts like Pt for HER. Sampling of binding energies and construction of a reaction probability model in the manner described in this study yields a new

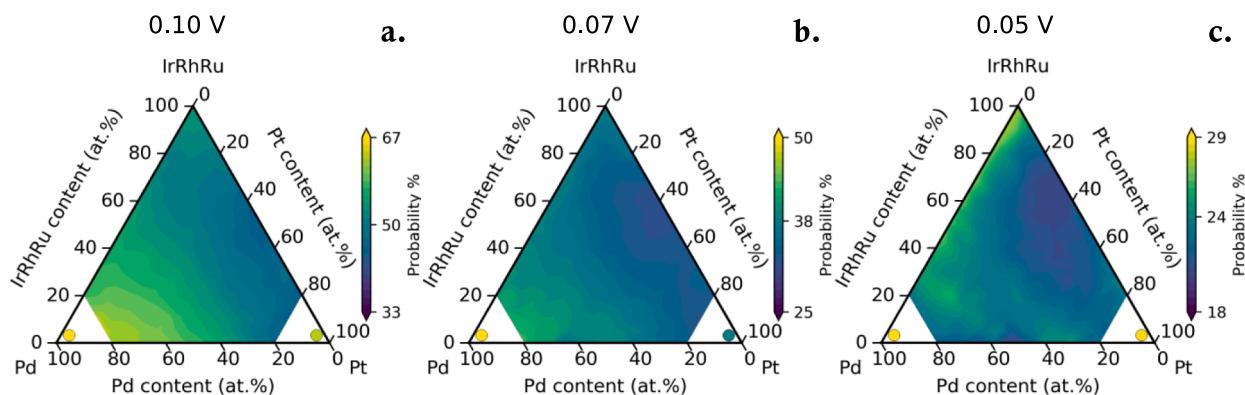


Fig. 7. Pseudo-ternary plots of probability model results of grid searches through all possible compositions with 0.05 M fraction steps for applied potentials **a.** 0.10 V, **b.** 0.07 V, and **c.** 0.05 V. Notice the unequal scaling of the color bars. As the adsorption energy distributions are sampled from HEAs the model is not suited for predicting the activity of alloys with high molar fractions of a single metal, thus the Pd and Pt corners are omitted above 80 % content. Color coded dots represent the performance of pure Pd and Pt in accordance with Fig. 6a.

exploration tool enabling the search within this new class of catalysts. Such investigation may find catalyst candidates that, though perhaps not exactly as well-suited for HER as Pt, exhibit a notable probability of reaction at low potentials. As acidic HER on Pt is still limited by mass transport even at ultra-low loading [21], perhaps the intrinsic activity need not be matched exactly to provide comparable performance. If only a fraction of the active sites on Pt(111) during HER in acid are sufficient to reach the mass-transport limitation, perhaps only a fraction of the reaction probability for Pt(111) may prove viable for HER on a HEA (111) surface.

3. Conclusion and outlook

The findings in this study suggest a critical role of hydrogen coverage when determining the rate of HER. Exploring the diverse properties of high-entropy alloys, we investigated the compositional space of multiple elements to identify optimal catalytic properties. Our analysis of (111) HEA surfaces with varying hydrogen coverages, utilizing distributions of binding energies, enabled the construction of a model that estimates the activity probability for H₂ formation as a function of applied potential. Through a systematic optimization of alloy compositions, we identified a set of promising catalyst candidates for the hydrogen evolution reaction by maximizing the reaction probability at specific potentials. Notably, our investigation accounted for the impact of hydrogen-hydrogen repulsion effects on the binding energy, revealing that the repulsion effect is more pronounced in HEAs compared to pure metals due to ligand effects. Furthermore, the observed distinct isotherm slopes in mean adsorption and desorption energy profiles may explain a potential hysteresis trend specific to HEAs. These insights underscore the potential of HEAs in advancing the development of efficient catalysts for HER applications.

Author contributions

F.C.Ø. wrote the main part and carried out the simulations and the modeling. J.R. and F.A.-P. contributed to the conceptual framework of the methodology as well as supervision, review, and editing.

CRediT authorship contribution statement

Frederik C. Østergaard: Writing – original draft, Investigation, Formal analysis, Data curation. **Frank Abild-Pedersen:** Writing – review & editing, Supervision, Methodology, Conceptualization. **Jan Rossmeisl:** Writing – review & editing, Supervision, Methodology, Conceptualization.

Declaration of competing interest

The authors declare that they have no known competing financial interests or personal relationships that could have appeared to influence the work reported in this paper.

Data availability

I have shared the link to data and scripts in the manuscript

Acknowledgements

F.C.Ø. and J.R. acknowledge support from the Danish National Research Foundation Center for High-Entropy Alloy Catalysis (CHEAC) DNRF-149. F.A.-P. acknowledges support from the US Department of Energy, Office of Science, Office of Basic Energy Sciences, Chemical Sciences, Geosciences, and Biosciences Division, Catalysis Science Program to the SUNCAT Center for Interface Science and Catalysis. J.R. acknowledges funding by the Deutsche Forschungsgemeinschaft (DFG, German Research Foundation) – SFB 1625, project number 506711657, subproject A01-Rossmeisl.

Appendix A. Supplementary material

Supplementary data to this article can be found online at <https://doi.org/10.1016/j.jcat.2024.115570>.

References

- [1] M. Pagliaro, A.G. Konstandopoulos, Solar Hydrogen, Royal Soc. Chem. (2012), <https://doi.org/10.1039/9781849733175>.
- [2] J. Kibsgaard, P.C.K. Vesborg, I. Chorkendorff, T.F. Jaramillo, J.K. Nørskov, P. G. Moses, J. Sehested, Power to Fuels and Chemicals Innovation Challenge, Technical University of Denmark, In Accelerating the clean energy revolution - perspectives on innovation challenges, 2018, pp. 73–80.
- [3] J.-W. Yeh, S.-K. Chen, S.-J. Lin, J.-Y. Gan, T.-S. Chin, T. Shun, C.-H. Tsau, S. Y. Chang, Nanostructured high-entropy alloys with multiple principal elements: novel alloy design concepts and outcomes, Adv. Eng. Mater. 6 (2004) 299–303, <https://doi.org/10.1002/adem.200300567>.
- [4] F. McKay, Y. Fang, O. Kizilkaya, P. Singh, D.D. Johnson, A. Roy, D.P. Young, P. T. Sprunger, J.C. Flake, W.A. Shelton, Y. Xu, CoCrFeNi high-entropy alloy as an enhanced hydrogen evolution catalyst in an acidic solution, J. Phys. Chem. C (2021), <https://doi.org/10.1021/acs.jpcc.1c03646>.
- [5] S. Schumacher, S. Baha, A. Savan, C. Andronescu, A. Ludwig, High-Throughput Discovery of Hydrogen Evolution Electrocatalysts in the complex solid solution system Co–Cr–Fe–Mo–Ni, J. Mater. Chem. A 10 (18) (2022) 9981–9987, <https://doi.org/10.1039/D2TA01652D>.
- [6] T.A.A. Batchelor, J.K. Pedersen, S.H. Winther, I.E. Castelli, K.W. Jacobsen, J. Rossmeisl, High-entropy alloys as a discovery platform for electrocatalysis, Joule 3 (3) (2019) 834–845, <https://doi.org/10.1016/j.joule.2018.12.015>.

- [7] J.K. Pedersen, C.M. Clausen, O.A. Krysiak, B. Xiao, T.A.A. Batchelor, T. Löffler, V. A. Mints, L. Banko, M. Arenz, A. Sazan, W. Schuhmann, A. Ludwig, J. Rossmeisl, Bayesian optimization of high-entropy alloy compositions for electrocatalytic oxygen reduction**, *Angew. Chemie* 133 (45) (2021) 24346–24354, <https://doi.org/10.1002/ange.202108116>.
- [8] C. Zlotea, M.A. Sow, G. Ek, J.-P. Couzinié, L. Perrière, I. Guillot, J. Bourgon, K. T. Møller, T.R. Jensen, E. Akiba, M. Sahlberg, Hydrogen sorption in TiZrNbHfTa high entropy alloy, *J. Alloy. Compd.* 775 (2019) 667–674, <https://doi.org/10.1016/j.jallcom.2018.10.108>.
- [9] J. Hu, H. Shen, M. Jiang, H. Gong, H. Xiao, Z. Liu, G. Sun, X. Zu, A DFT study of hydrogen storage in high-entropy alloy TiZrHfScMo, *Nanomaterials* (2019), <https://doi.org/10.3390/nano9030461>.
- [10] K.R. Cardoso, V. Roche, A.M. Jorge Jr, F.J. Antikeira, G. Zepon, Y. Champion, Hydrogen storage in MgAlTiFeNi high entropy alloy, *J. Alloy. Compd.* 858 (2021) 158357, <https://doi.org/10.1016/j.jallcom.2020.158357>.
- [11] C.M. Moore, J.A. Wilson, M.J.D. Rushton, W.E. Lee, J.O. Astbury, S. C. Middleburgh, Hydrogen accommodation in the TiZrNbHfTa High entropy alloy, *Acta Mater.* 229 (2022) 117832, <https://doi.org/10.1016/j.actamat.2022.117832>.
- [12] R. Parsons, The rate of electrolytic hydrogen evolution and the heat of adsorption of hydrogen, *Trans. Faraday Soc.* 54 (1958) 1053–1063, <https://doi.org/10.1039/TF9585401053>.
- [13] E. Santos, In search of lost descriptors: correlations and their risks, *Curr. Opin. Electrochem.* 37 (2023) 101194, <https://doi.org/10.1016/j.coelec.2022.101194>.
- [14] A. Ciotti, M. García-Melchor, The importance of surface coverages in the rational design of electrocatalysts, *Curr. Opin. Electrochem.* 42 (2023) 101402, <https://doi.org/10.1016/j.coelec.2023.101402>.
- [15] T. Li, A. Ciotti, M. Rahaman, C.W.S. Yeung, M. García-Melchor, E. Reisner, Driving Electrochemical Organic Hydrogenation on Metal Catalysts by Tailoring Hydrogen Surface Coverages (2023), <https://doi.org/10.26434/chemrxiv-2023-146f9>.
- [16] F.C. Østergaard, A. Bagger, J. Rossmeisl, Predicting catalytic activity in hydrogen evolution reaction, *Curr. Opin. Electrochem.* 35 (2022) 101037, <https://doi.org/10.1016/j.coelec.2022.101037>.
- [17] Q. Shi, R. Sun, Adsorption manners of hydrogen on Pt(100), (110) and (111) surfaces at high coverage, *Comput. Theor. Chem.* 1106 (2017) 43–49, <https://doi.org/10.1016/j.comptc.2017.02.024>.
- [18] M.D. Pohl, S. Watzel, F. Calle-Vallejo, A.S. Bandarenka, Nature of highly active electrocatalytic sites for the hydrogen evolution reaction at Pt electrodes in acidic media, *ACS Omega* 2 (11) (2017) 8141–8147, <https://doi.org/10.1021/acsomega.7b01126>.
- [19] F. Calle-Vallejo, J. Tymoczko, V. Colic, Q.H. Vu, M.D. Pohl, K. Morgenstern, D. Loffreda, P. Sautet, W. Schuhmann, A.S. Bandarenka, Finding optimal surface sites on heterogeneous catalysts by counting nearest neighbors, *Science* (80-) 350 (6257) (2015) 185–189, <https://doi.org/10.1126/science.aab3501>.
- [20] C.M. Clausen, T.A.A. Batchelor, J.K. Pedersen, J. Rossmeisl, What atomic positions determines reactivity of a surface? long-range, directional ligand effects in metallic alloys, *Adv. Sci.* 8 (9) (2021) 2003357, <https://doi.org/10.1002/adv.202003357>.
- [21] J.N. Hansen, H. Prats, K.K. Toudahl, N. Mørch Secher, K. Chan, J. Kibsgaard, I. Chorkendorff, Is there anything better than Pt for HER? *ACS Energy Lett.* 6 (4) (2021) 1175–1180, <https://doi.org/10.1021/acsenrgylett.1c00246>.
- [22] Xu, W.; Diesen, E.; He, T.; Reuter, K.; Margraf, J. *Discovering High Entropy Alloy Electrocatalysts in Vast Composition Spaces with Multi-Objective Optimization*; 2023. doi: 10.26434/chemrxiv-2023-d563d.
- [23] J. Li, J.H. Stenlid, T. Ludwig, P.S. Lamoureux, F. Abild-Pedersen, Modeling potential-dependent electrochemical activation barriers: revisiting the alkaline hydrogen evolution reaction, *J. Am. Chem. Soc.* 143 (46) (2021) 19341–19355, <https://doi.org/10.1021/jacs.1c07276>.
- [24] S. Trasatti, Work function, electronegativity, and electrochemical behaviour of metals: III. electrolytic hydrogen evolution in acid solutions, *J. Electroanal. Chem. Interfacial Electrochem.* 39 (1) (1972) 163–184, [https://doi.org/10.1016/S0022-0728\(72\)80485-6](https://doi.org/10.1016/S0022-0728(72)80485-6).
- [25] J.K. Nørskov, T. Bligaard, A. Logadottir, J.R. Kitchin, J.G. Chen, S. Pandalov, U. Stimming, Trends in the exchange current for hydrogen evolution, *J. Electrochem. Soc.* 152 (3) (2005) J23, <https://doi.org/10.1149/1.1856988>.
- [26] A.R. Zeradjanin, J.-P. Grote, G. Polymeros, K.J.J. Mayrhofer, A Critical review on hydrogen evolution electrocatalysis: re-exploring the volcano-relationship, *Electroanalysis* 28 (10) (2016) 2256–2269, <https://doi.org/10.1002/elan.201600270>.
- [27] A.R. Zeradjanin, G. Polymeros, C. Toparli, M. Ledendecker, N. Hodnik, A. Erbe, M. Rohwerder, F. La Mantia, What Is the trigger for the hydrogen evolution reaction? – towards electrocatalysis beyond the sabatier principle, *PCCP* 22 (16) (2020) 8768–8780, <https://doi.org/10.1039/D0CP01108H>.
- [28] E. Skúlason, G. Karlberg, J. Rossmeisl, T. Bligaard, J. Greeley, H. Jonsson, J. Nørskov, Density functional theory calculations for the hydrogen evolution reaction in an electrochemical double layer on the Pt(111) electrode, *PCCP* 9 (2007) 3241–3250, <https://doi.org/10.1039/b700099e>.
- [29] J. Cheng, P. Hu, P. Ellis, S. French, G. Kelly, C.M. Lok, Brønsted–evans–polanyi relation of multistep reactions and volcano curve in heterogeneous catalysis, *J. Phys. Chem. C* 112 (5) (2008) 1308–1311, <https://doi.org/10.1021/jp711191j>.
- [30] J.J. Mortensen, L.B. Hansen, K.W. Jacobsen, Real-space grid implementation of the projector augmented wave method, *Phys. Rev. B* 71 (3) (2005) 35109, <https://doi.org/10.1103/PhysRevB.71.035109>.
- [31] J. Enkovaara, C. Rostgaard, J.J. Mortensen, J. Chen, M. Dulak, L. Ferrighi, J. Gavnholt, C. Glinsvad, V. Haikola, H.A. Hansen, H.H. Kristoffersen, M. Kuisma, A.H. Larsen, L. Lehtovaara, M. Ljungberg, O. Lopez-Acevedo, P.G. Moses, J. Ojanen, T. Olsen, V. Petzold, N.A. Romero, J. Stausholm-Møller, M. Strange, G. A. Tritsarlis, M. Vanin, M. Walter, B. Hammer, H. Häkkinen, G.K.H. Madsen, R. M. Nieminen, J.K. Nørskov, M. Puska, T.T. Rantala, J. Schiøtz, K.S. Thygesen, K. W. Jacobsen, Electronic structure calculations with GPAW: a real-space implementation of the projector augmented-wave method, *J. Phys. Condens. Matter* 22 (25) (2010) 253202, <https://doi.org/10.1088/0953-8984/22/25/253202>.
- [32] B. Hammer, L.B. Hansen, J.K. Nørskov, Improved adsorption energetics within density-functional theory using revised Perdew-Burke-Ernzerhof functionals, *Phys. Rev. B* 59 (11) (1999) 7413–7421, <https://doi.org/10.1103/PhysRevB.59.7413>.
- [33] A.H. Larsen, J.J. Mortensen, J. Blomqvist, I.E. Castelli, R. Christensen, M. Dulak, J. Friis, M.N. Groves, B. Hammer, C. Hargus, E.D. Hermes, P.C. Jennings, P. B. Jensen, J. Kermode, J.R. Kitchin, E.L. Kolsbjerg, J. Kubal, K. Kaasbjerg, S. Lysgaard, J.B. Maronsson, T. Maxson, T. Olsen, L. Pastewka, A. Peterson, C. Rostgaard, J. Schiøtz, O. Schütt, M. Strange, K.S. Thygesen, T. Vegge, L. Vilhelmsen, M. Walter, Z. Zeng, K.W. Jacobsen, The atomic simulation environment - a python library for working with atoms, *J. Phys. Condens. Matter* 29 (27) (2017) 273002, <https://doi.org/10.1088/1361-648x/aa680e>.
- [34] P.W. Atkins, *Physical Chemistry*, Oxford University Press, Oxford; Melbourne; Tokyo, 1998.
- [35] Nguyen, V., Gupta, S., Rana, S., Li, C., Venkatesh, S. Regret for Expected Improvement over the Best-Observed Value and Stopping Condition. In *Proceedings of the Ninth Asian Conference on Machine Learning*; Zhang, M.-L., Noh, Y.-K., Eds.; Proceedings of Machine Learning Research; PMLR: Yonsei University, Seoul, Republic of Korea, 2017, 77, pp 279–294.
- [36] C.M. Clausen, M.L.S. Nielsen, J.K. Pedersen, J. Rossmeisl, Ab initio to activity: machine learning-assisted optimization of high-entropy alloy catalytic activity, *High Entropy Alloy. Mater.* (2022), <https://doi.org/10.1007/s44210-022-00006-4>.
- [37] J. Rossmeisl, J.K. Nørskov, C.D. Taylor, M.J. Janik, M. Neurock, Calculated phase diagrams for the electrochemical oxidation and reduction of water over Pt(111), *J. Phys. Chem. B* 110 (43) (2006) 21833–21839, <https://doi.org/10.1021/jp0631735>.
- [38] E. Skúlason, V. Tripkovic, M.E. Björketun, S. Gudmundsdóttir, G. Karlberg, J. Rossmeisl, T. Bligaard, H. Jónsson, J.K. Nørskov, Modeling the electrochemical hydrogen oxidation and evolution reactions on the basis of density functional theory calculations, *J. Phys. Chem. C* 114 (42) (2010) 18182–18197, <https://doi.org/10.1021/jp1048887>.
- [39] W. Sheng, H.A. Gasteiger, Y. Shao-Horn, Hydrogen oxidation and evolution reaction kinetics on platinum: acid vs alkaline electrolytes, *J. Electrochem. Soc.* 157 (11) (2010) B1529, <https://doi.org/10.1149/1.3483106>.
- [40] N. Danilovic, R. Subbaraman, D. Strmcnik, K.-C. Chang, A.P. Paulikas, V. R. Stamenkovic, N.M. Markovic, Enhancing the alkaline hydrogen evolution reaction activity through the bifunctionality of Ni(OH)₂/metal catalysts, *Angew. Chemie Int. Ed.* 51 (50) (2012) 12495–12498, <https://doi.org/10.1002/anie.201204842>.
- [41] S. Siahrostami, A. Verdager-Casadevall, M. Karamad, D. Deiana, P. Malacrida, B. Wickman, M. Escudero-Escribano, E.A. Paoli, R. Frydendal, T.W. Hansen, I. Chorkendorff, I.E.L. Stephens, J. Rossmeisl, Enabling Direct H₂O₂ production through rational electrocatalyst design, *Nat. Mater.* 12 (12) (2013) 1137–1143, <https://doi.org/10.1038/nmat3795>.
- [42] S. Siahrostami, S.J. Villegas, A.H. Bagherzadeh Mostaghimi, S. Back, A.B. Farimani, H. Wang, K.A. Persson, J. Montoya, A review on challenges and successes in atomic-scale design of catalysts for electrochemical synthesis of hydrogen peroxide, *ACS Catal.* 10 (14) (2020) 7495–7511, <https://doi.org/10.1021/acscatal.0c01641>.
- [43] F.A. Lewis, The palladium-hydrogen system, *Platin. Met. Rev.* 26 (1) (1982) 20–27.
- [44] T. Scheler, O. Degtyareva, M. Marqués, C.L. Guillaume, J.E. Proctor, S. Evans, E. Gregoryanz, Synthesis and properties of platinum hydride, *Phys. Rev. B* 83 (21) (2011) 214106, <https://doi.org/10.1103/PhysRevB.83.214106>.
- [45] D.Y. Kim, R.H. Scheicher, C.J. Pickard, R.J. Needs, R. Ahuja, Predicted formation of superconducting platinum-hydride crystals under pressure in the presence of molecular hydrogen, *Phys. Rev. Lett.* 107 (11) (2011) 117002.
- [46] Lewis, F. A.; McKee, S. G. Hydride formation by nickel, palladium and platinum; Veziroğlu, T. N. B. T.-M. S., Ed.; Pergamon, 1982; pp 423–436. doi: 10.1016/B978-0-08-027311-2.50043-7.
- [47] I.T. McCrum, M.T.M. Koper, The role of adsorbed hydroxide in hydrogen evolution reaction kinetics on modified platinum, *Nat. Energy* 5 (11) (2020) 891–899, <https://doi.org/10.1038/s41560-020-00710-8>.
- [48] V. Giulimondi, A. Ruiz-Ferrando, A. Clark, S. Kaiser, F. Krumeich, A. Martín, N. López, J. Pérez-Ramírez, Catalytic synergies in bimetallic RuPt single-atom catalysts via speciation control, *Adv. Funct. Mater.* 32 (2022), <https://doi.org/10.1002/adfm.202206513>.
- [49] K.S. Exner, Does a thermoneutral electrocatalyst correspond to the apex of a volcano plot for a simple two-electron process? *Angew. Chemie Int. Ed.* 59 (26) (2020) 10236–10240, <https://doi.org/10.1002/anie.202003688>.